Functional and molecular insights into the role of Sae2 C-terminus in the activation of MRX endonuclease

Chiara Vittoria Colombo [iD][†], **Erika Casari** [iD][†], **Marco Gnugnoli** [iD], **Flavio Corallo, Renata Tisi** [iD]* and **Maria Pia Longhese** [iD]*

Dipartimento di Biotecnologie e Bioscienze, Università degli Studi di Milano - Bicocca, 20126 Milano, Italy

*To whom correspondence should be addressed. Tel: +39 0264483425; Email: mariapia.longhese@unimib.it
Correspondence may also be addressed to Renata Tisi. Email: renata.tisi@unimib.it
†The first two authors should be regarded as Joint First Authors.

Abstract

The yeast Sae2 protein, known as CtIP in mammals, once phosphorylated at Ser267, stimulates the endonuclease activity of the Mre11-Rad50-Xrs2 (MRX) complex to cleave DNA ends that possess hairpin structures or protein blocks, such as the Spo11 transesterase or trapped topoisomerases. Stimulation of the Mre11 endonuclease by Sae2 depends on a Rad50–Sae2 interaction, but the mechanism by which this is achieved remains to be elucidated. Through genetic studies, we show that the absence of the last 23 amino acids from the Sae2 C-terminus specifically impairs MRX-dependent DNA cleavage events, while preserving the other Sae2 functions. Employing AlphaFold3 protein structure predictions, we found that the Rad50–Sae2 interface involves not only phosphorylated Ser267 but also the phosphorylated Thr279 residue and the C-terminus of Sae2. This region engages in multiple interactions with residues that are mutated in *rad50-s* mutants, which are known to be specifically defective in the processing of Spo11-bound DNA ends. These interactions are critical for stabilizing the association between Sae2 and Rad50, thereby ensuring the correct positioning of Mre11 in its active endonucleolytic state.

Graphical abstract
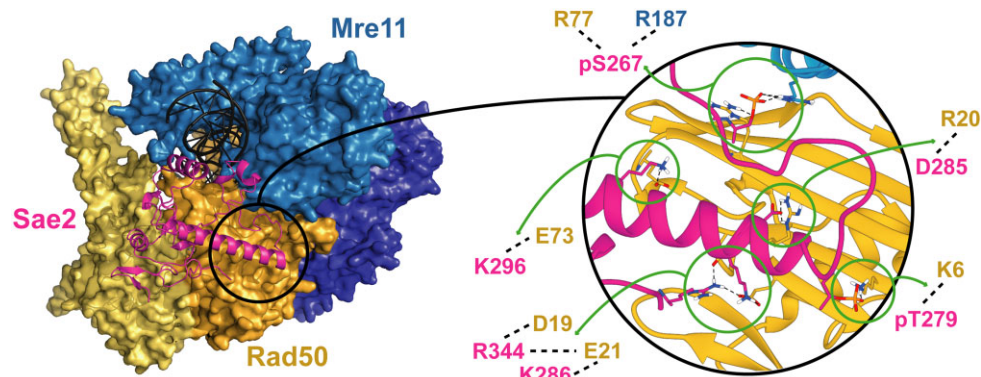
Introduction

DNA double-strand breaks (DSBs) represent a severe form of DNA damage that can be repaired by non-homologous end-joining (NHEJ) or homologous recombination (HR). NHEJ directly ligates DNA ends (1), while HR employs a homologous template, typically the sister chromatid, for repair (2). The essential step in HR is the degradation (resection) of the 5′-terminated DNA strands at both DSB ends to generate 3′-end single-stranded DNA (ssDNA) overhangs that allow homologous pairing and strand invasion (3). The generation of DNA DSBs also activates a checkpoint response, with Mec1 and Tel1 proteins (ATR and ATM in mammals, respectively)

serving as apical protein kinases (4). Upon activation by damaged DNA, Tel1 and Mec1 transduce checkpoint signals to the downstream kinase Rad53, whose activation depends on the Rad9 protein (53BP1 in mammals) (5–7).

The evolutionarily conserved Mre11-Rad50-Xrs2/NBS1 complex (MRX in *Saccharomyces cerevisiae* and MRN in mammals) plays a crucial role in the repair of DNA DSBs. It initiates the resection of DNA DSBs and signals their presence by recruiting and activating the checkpoint kinase Tel1/ATM (8). Rad50 is an ATPase from the ABC transporter family, while Mre11 exhibits both 3′-5′ exonuclease and endonuclease activities (9–11). The Mre11 subunit dimerizes and

interacts with two Rad50 nucleotide-binding domains, forming a globular head that possesses DNA binding, nuclease and ATPase activities (12–14). From this head domain, two long Rad50 anti-parallel coiled-coils joined by a Zn^{2+}-hook extend to form a ring- or rod-like structure (15,16).

The current model for DSB resection proposes that Mre11 initially clips the 5′-terminated strands on either side of a DNA DSB. This is followed by 3′-5′ exonucleolytic processing back toward the DNA ends, generating 100–300 nucleotides of ssDNA. Subsequent processing occurs in the 5′-3′ direction away from the DSB end by the nuclease Exo1 or Dna2 in cooperation with the helicase Sgs1/BLM (17–25). In *Saccharomyces cerevisiae*, the MRX-mediated end clipping is essential for processing DSB ends that exhibit non-canonical structures, such as DNA hairpins or protein adducts, including trapped topoisomerases or Spo11, which generates meiotic DSBs in a programmed manner and remain covalently attached to the 5′ ends (22,26–28). Conversely, MRX is not required for the processing of clean DNA breaks, such as those created by endonucleases, where the DNA ends can be directly resected by Exo1 or Dna2-Sgs1 without the need for Mre11 nuclease activity (29).

Rad50 ATPase activity drives conformational changes in the MRX complex that regulate its functions at DSBs (30–37). In its ATP-bound state, the Rad50 dimer forms a DNA-binding platform that blocks the access of Mre11 to double-stranded DNA (resting state), thereby inhibiting its nuclease activity. Upon ATP hydrolysis, the nucleotide-binding domains of Rad50 dissociate, allowing the Mre11 subunits to move to one side of Rad50. This repositioning (cutting state) enables one Mre11 subunit to engage with a bound DNA substrate and carry out the endonucleolytic cleavage.

In both yeast and mammals, Sae2 (CtIP in mammals) is a critical cofactor of the MRX/MRN complex. Sae2 and CtIP are phosphorylated during the cell-cycle and following DNA damage (38–43). Particularly, following phosphorylation by cyclin-dependent kinases (CDKs) at S267 in Sae2 (40) and T847 in CtIP (41), Sae2/CtIP interacts with Rad50 and stimulates the Mre11 endonuclease activity (42). A *sae2* mutant, in which S267 is non-phosphorylatable (*sae2-S267A*), shows deficient MRX endonuclease activation, while a phospho-mimicking *sae2* mutant (*sae2-S267E*) is proficient in supporting MRX-mediated cleavage events (42). This stimulation of Mre11 endonuclease by Sae2 depends on Rad50-Sae2 interaction. In fact, the *S. cerevisiae rad50-K81I* allele, which belongs to a series of separation-of-function *rad50-s* mutants originally identified for their defects in processing Spo11-bound DSBs (44), encodes a Rad50 variant that cannot interact with phosphorylated Sae2 (42). The amino acid changes carried by the *rad50-s* alleles (K6, S14, R20, E21, G39, K40, V63, Q79, N97 and Q99) are located at the N-terminus of Rad50, suggesting that this region likely serves as the binding interface for phosphorylated Sae2 (45). Although the mechanism by which Sae2/CtIP activates Mre11 endonuclease is still to be fully understood, the activation is dependent on ATP hydrolysis by Rad50 (25,42), suggesting that Sae2 likely promotes Mre11 endonuclease activity by stabilizing a nucleolytically active Mre11-Rad50 conformation.

Sae2 not only stimulates the endonuclease activity of the MRX complex but also plays a crucial role in negatively regulating Rad53 activation. The absence of Sae2 leads to an increased association of MRX and Tel1 at DNA DSBs, result-ing in the accumulation of Rad9. Rad9 persistence impairs DSB resection by inhibiting Dna2-Sgs1 processing and leads to permanent cell-cycle arrest due to the hyperactivation of Rad53 (46–50). Interestingly, despite both Mre11 and Tel1 still accumulating at DSBs when Mre11 nuclease activity is abolished, neither increased Rad9 association nor Rad53 hyperactivation is observed (51). This indicates that the Sae2 role in dampening the DNA damage checkpoint is independent of Mre11 nuclease activation.

Here we explore the role of Sae2 in supporting MRX endonuclease activity. By searching for *sae2* alleles that reduce DNA hairpin resolution, we found that the absence of its last 23 amino acids impairs Sae2 ability to support MRX-mediated DNA cleavage, whereas it still preserves Sae2 function in limiting Rad53 activation. By using AlphaFold3 protein structure predictor, we show that the modeled Rad50–Sae2 interface includes both the phosphorylated S267 and T279 residues, along with its adjacent amino acids, and the C-terminus of Sae2, which is not required for Sae2 binding to the MRX complex, but it is crucial for the endonuclease activity of the complex.

Materials and methods

Search for *sae2* alleles that reduce hairpin resolution

To search for *sae2* alleles that reduce hairpin resolution, DNA from a strain carrying the *TRP1* gene located 122 bp downstream of the *SAE2* stop codon was used as a template to amplify by low-fidelity PCR a *SAE2* region spanning from position −54 to + 212 bp from the *SAE2* coding sequence. Thirty independent PCR reaction mixtures were prepared, each containing 5 U GoTaq G2 Flexi DNA polymerase (Promega), 10 ng genomic DNA, 500 ng each primer, 0.5 mM each dNTP (dATP, dTTP, dCTP), 0.1 mM dGTP, 0.5 mM $MnCl_2$, 10 mM Tris-HCl (pH 8.3), 50 mM KCl and 3 mM $MgCl_2$. The resulting PCR amplification products, containing the *SAE2* coding sequence and the *TRP1* marker gene, were used to transform an HS21 strain to replace the wild-type *SAE2* sequence with the mutagenized DNA fragments. Transformant clones were selected on synthetic complete (SC) medium without tryptophan and then assayed by drop test for decreased viability on SC medium without lysine compared to wild-type cells. Among them, the clones that showed camptothecin (CPT) and phleomycin resistance compared to *sae2Δ* cells were chosen for further characterization.

Yeast strains, plasmids, and growth condition

S. cerevisiae is the experimental model used in this study. Strain genotypes are listed in Supplementary Table S1. Strain JKM139, used to detect DSB resection, was kindly provided by J. Haber (Brandeis University, Waltham, USA). Strain HS21, used to detect hairpin resolution, was kindly provided by M.A. Resnick (NIH, Durham, USA). Gene disruptions and tag fusions were generated by one-step PCR and standard yeast transformation procedures. Primers used for disruptions and gene tagging are listed in Supplementary Table S2. Cells were grown in YEP medium (1% yeast extract, 2% bactopeptone) supplemented with 2% glucose (YEPD), 2% raffinose (YEPR), or 2% raffinose and 3% galactose (YEPRG). All experiments were performed at 26°C.

Chromatin immunoprecipitation and qPCR

YEPR exponentially growing cell cultures of JKM139 derivative strains, carrying the HO cut site at the *MAT* locus, were transferred to YEPRG at time zero, as previously described (52). Crosslinking was performed with 1% formaldehyde for 5 min (Mre11) and 10 min (Rad9 and Tel1). The reaction was stopped by adding 0.125 M glycine for 5 min. Immunoprecipitation (IP) was performed by incubating samples with Dynabeads Protein G (ThermoFisher Scientific) for 3 h at 4°C in the presence of 5 μg anti-HA (12CA5) or anti-Myc (9E10) antibodies. Quantification of immunoprecipitated DNA was achieved by qPCR on a Bio-Rad CFX Connect™ Real-Time System apparatus and Bio-Rad CFX Maestro 1.1 software. Triplicate samples in 20 μl reaction mixture containing 10 ng of template DNA, 300 nM for each primer, 2 × SsoFast™ EvaGreen supermix (Bio-Rad #1 725 201) (2 × reaction buffer with dNTPs, Sso7d-fusion polymerase, MgCl2, EvaGreen dye and stabilizers) were run in white 96-well PCR plates Multiplate™ (Bio-Rad MLL9651). The qPCR program was as follows: step 1, 98°C for 2 min; step 2, 90°C for 5 s; step 3, 60°C for 15 s; step 4, return to step 2 and repeat 40 times. At the end of the cycling program, a melting program (from 65 to 95°C with a 0.5°C increment every 5 s) was run to test the specificity of each qPCR. Data are expressed as fold enrichment at the HO-induced DSB over that at the non-cleaved *ARO1* locus, after normalization of the chromatin immunoprecipitation (ChIP) signals to the corresponding input for each time point. Oligonucleotides used for qPCR analyses are listed in Supplementary Table S3.

Western blotting

Protein extracts for western blot analysis were prepared by trichloroacetic acid (TCA) precipitation and separated on 10% polyacrylamide gels. Rad53 was detected by using anti-Rad53 polyclonal antibodies (ab104232 from Abcam). Epitope-tagged Mre11, Tel1, Rad9 and Sae2 were detected by using anti-HA (12CA5) or anti-Myc antibodies (Ab32 from Abcam).

Hairpin opening assay

The rate of Lys$^+$ recombinants was derived from the median recombination frequency determined from 10 different isolates of each strain, as previously described (27). Three trials were performed, and the mean recombination rate was calculated.

Co-immunoprecipitations

Rad53-Rad9 co-IP was performed as previously described (6). Briefly, cells were broken in 400 μl of buffer containing PBS + 1% Triton X-100, 10% glycerol and protease inhibitor cocktail, followed by IP of the clarified protein extracts with 50 μl of Protein A-sepharose and 5 μg anti-HA (12CA5) antibodies for 2 hours at 4°C. The resins were washed three times with breaking buffer and three times with 1× PBS. Bound proteins were visualized by western blotting with an anti-Rad53 (kindly provided by J. Diffley, The Francis Crick Institute, London, UK) (1:2500) or an anti-HA (12CA5) (1:2000) antibody after electrophoresis on a 10% SDS-polyacrylamide gel. To perform Rad50-Sae2 co-IPs cells were broken in 400 μl of buffer containing 50 mM HEPES pH 7.5, 140 mM NaCl, 1 mM EDTA pH 7.5, 10% glycerol, 1 mM sodium ortho-

vanadate, 60 mM β-glycerophosphate, 1 mM phenylmethylsulfonyl fluoride and protease inhibitor cocktail (Roche Diagnostics), as previously described (53). An equal volume of breaking buffer was added to clarified protein extracts and tubes were incubated for 2 h at 4°C with 50 μl of Protein G-Dynabeads and 5 μg anti-HA (12CA5) antibodies. The resins were then washed three times with 1 mL of PBS 1× and once with 1 mL breaking buffer. Bound proteins were visualized by western blotting with an anti-Myc (9E10) (1:1000) or an anti-HA (12CA5) (1:2000) antibody after electrophoresis on a 7.5% or 10% SDS-polyacrylamide gel.

DSB resection

YEPR exponentially growing cell cultures of JKM139 derivative strains, carrying the HO-cut site at the *MAT* locus, were transferred to YEPRG at time zero. *Ssp*I-digested genomic DNA was run on an alkaline agarose gel and visualized after hybridization with an RNA probe that anneals with the unresected strand on one side of the HO-induced DSB, as previously described (54). This probe was obtained by *in vitro* transcription using Promega Riboprobe System-T7 and plasmid pML514 as a template. Plasmid pML514 was constructed by inserting in the pGEM7Zf vector a 900-bp fragment containing part of the *MAT* locus (coordinates 200 870 to 201 587 on chromosome III) (55). Quantitative analysis of DSB resection was performed by calculating the ratio of band intensities for ssDNA and the total amount of DSB products. The resection efficiency was normalized with respect to the HO cleavage efficiency for each time point. Densitometric analysis of band intensities was performed using Scion Image Beta 4.0.2.

Structural bioinformatics

We employed AlphaFold2 multimer v3 on Colabfold (56) to model the C-terminal region of Sae2 (aa 181–345) with the S267E mutation, alongside a truncated version of Rad50 that omitted the amino acids 214–1107 of the coiled-coil region to improve computational efficiency. Template mode was set to the pdb100 database, with msa_mode as mmseqs2_uniref_env in unpaired_paired pair_mode, which pairs the available sequences for the same species using a greedy pairing strategy. Default sample settings were applied (max_msa automatic, num_seeds = 1). The number of recycles was set at 20 with a tolerance of 0.5. One relaxed model was obtained with a maximum of 200 relax iterations using amber. The top-scoring model obtained an average plDDT of 76.7, pTM = 0.75 and ipTM = 0.717. The residue plDDT and the sequence coverage provided by AlphaFold2 are shown in Supplementary Figure S1A and B. The AlphaFold3 (56) server was used to model the same 181–345 amino-acid region of S267-phosphorylated and T279-phosphorylated Sae2, together with Rad50 (deleted of the aa 214–1107 extension of the coiled-coil region) and Mre11 (aa 1–416). The top score model obtained an average pTM of 0.64 and ipTM of 0.52. Single-chain and chain-to-chain pTM, ipTM and the expected error scores calculated by AlphaFold3 are shown in Supplementary Table S4. The residue plDDT and the expected error of the AlphaFold3 model are shown in Supplementary Figure S1C and D. AlphaFold3-built models for Rad50 and Mre11 dimers were also obtained, with the same sequence portions described above, achieving a plDDT score greater than 90 across all models. These models were used to reconstruct the cutting state Mre11–Rad50–Sae2 com-

plex by superimposing one of the monomers from the dimers on the Mre11 and Rad50 proteins in the Mre11–Rad50–Sae2 complex. Finally, a DNA molecule was added by superposition of the resolved structure of the cutting state in the *E. coli* homolog complex (PDB ID: 7Z03) (37). A model for human CtIP (aa 671–897) phosphorylated on T847 together with a Rad50 dimer (with the coiled-coil region between amino acids 254–1057 removed), and Mre11 (aa 1–537), spanning the endonuclease, capping and Rad50-binding domains, was obtained using AlphaFold3. The top-scored model obtained an average pTM of 0.57 and ipTM of 0.48. The single-chain and chain-to-chain pTM, ipTM and the expected error scores calculated by AlphaFold3 are shown in Supplementary Table S5. The residue plDDT and the expected error for this model are shown in Supplementary Figure S2A and B. The same procedure described for the reconstruction of *S. cerevisiae* Mre11–Rad50–Sae2 complex in the cutting state on DNA was adopted to reconstruct the human Mre11–Rad50–CtIP complex on DNA in the cutting state conformation (Supplementary Figure S3A and B). A model for the 1–65 aa N-terminal aa of Rif2 was obtained together with a truncated version of Rad50 that omitted the amino acids 214–1107 (Supplementary Figure S4A-C). The top-scored model obtained an average pTM of 0.75 and ipTM of 0.69. The top score models were refined by adding the correct ionization and missing hydrogen atoms in Maestro suite (Schrödinger, LLC, New York, NY, 2024) and by proceeding to energy minimization of the interface residues conformations using AMBER force field (57) with implicit solvent, using the PRCG method and a gradient convergence threshold of 0.05. Superposition of structures was performed using the align function in UCSF Chimera (58). Polar interactions and pi–cation interactions were analyzed using UCSF Chimera and the Maestro suite, respectively. Visualization of structures was prepared with UCSF Chimera or Pymol.

Statistical analysis

Statistical analysis was performed using Microsoft Excel Professional 365 software. *P*-values were determined by using an unpaired two-tailed *t*-test. No statistical methods or criteria were used to estimate the size or to include or exclude samples.

Results

Identification of *sae2* alleles specifically impaired in hairpin resolution

Stimulation of the endonuclease activity of the MRX complex requires the binding of phosphorylated Sae2, allowing Mre11 to cleave DNA hairpin structures and the 5′-terminated strands of DNA DSBs (22,27,28,42,59). To understand how Sae2 activates the Mre11 endonuclease, we searched for *sae2* mutants specifically defective in repairing DNA hairpin structures. Hairpin resolution was assessed using the genetic assay developed by Lobachev et al., where inverted Alu elements inserted in the *LYS2* gene on chromosome II stimulate ectopic recombination with a truncated *lys2* gene (*lys2-Δ5′*) on chromosome III, resulting in Lys⁺ recombinants (Figure 1A). This recombination requires Mre11 endonuclease and Sae2, which are thought to cleave and subsequently repair the hairpin-capped DSB generated upon extrusion and processing of the inverted Alu repeats (27).

The *SAE2* gene was amplified using low-fidelity PCR, and the linear PCR products were used to transform a haploid strain carrying the *lys2::AluIR* and *lys2-Δ5′* ectopic recombination reporters to replace the wild-type *SAE2* sequence with the mutagenized DNA fragments. The transformants were then tested by drop tests for their ability to generate Lys⁺ prototrophs compared to wild-type cells.

Previous studies have shown that, although both the nuclease-defective *mre11-H125N* (hereafter referred to as *mre11-nd*) and *sae2Δ* alleles show similar defects in DNA hairpin cleavage, *sae2Δ* cells display increased sensitivity to DNA damaging agents compared to *mre11-nd* cells (47,51). This increased DNA damage sensitivity of *sae2Δ* cells is partly due to the enhanced retention of Rad9 at DSBs, which leads to prolonged phosphorylation and activation of Rad53 (46,47,51). Thus, to identify *sae2* mutants specifically defective in stimulating Mre11 nuclease activity, we focused on clones that not only generated fewer Lys⁺ prototrophs than wild-type cells but also showed greater resistance to CPT and phleomycin (phleo) compared to *sae2Δ* cells.

This analysis enabled us to identify the *sae2-L302**, and *sae2-L323** alleles, each carrying a single nucleotide change that introduces a stop codon in place of Leu302 or Leu323, respectively, and the *sae2-S267P* and *sae2-D285G* alleles, carrying single nucleotide substitutions that result in the replacement of Ser267 with Pro or Asp285 with Gly, respectively (Figure 1B). All the identified *sae2* mutants showed fewer Lys⁺ prototrophs compared to wild-type cells and increased resistance to CPT and phleomycin compared to *sae2Δ* cells (Figure 1B). Furthermore, they all showed decreased rates of Lys⁺ recombinants (Figure 1C), suggesting that these alleles are specifically defective in repairing hairpin DNA structures.

During meiosis, Spo11 cleaves DNA strands at recombination hotspots to initiate recombination and remains covalently bound to the 5′ end of the cleaved strands (22,26,28). In *S. cerevisiae*, Sae2-stimulated MRX endonuclease activity is absolutely required for the removal of Spo11-bound oligonucleotides from meiotic DSBs to allow DSB resection and subsequent repair by HR. Thus, to determine if the reduced rate of Lys⁺ recombinants in the *sae2* mutants was due to DNA cleavage defects, the *sae2* alleles were tested for defects in meiosis. Similar to *sae2Δ* and *mre11-nd*, all the diploid strains homozygous for the *sae2* mutations failed to sporulate, as expected from cells that still form meiotic DSBs but are impaired in Spo11 removal (Figure 1D).

The lack of the Sae2 C-terminus maintains Sae2 functions in resection of an endonuclease-induced DSB

Among the identified *sae2* alleles, the *sae2-S267P* mutation alters the Ser267 residue, whose phosphorylation is required to stimulate MRX endonuclease activity (42). Although replacing the serine residue with proline can affect secondary structure, rather than just eliminating the phosphorylation site, it is worth noting that *sae2-S267P* cells, while showing decreased rates of Lys⁺ recombinants (Figure 1C), exhibit increased resistance to CPT and phleomycin compared to *sae2Δ* cells (Figure 1B), suggesting that this allele maintains most of Sae2 functions.

The other *sae2* mutations occur in the carboxy-terminal part of Sae2, with two mutations leading to the deletion of the Sae2 C-terminus to varying extents, highlighting the critical
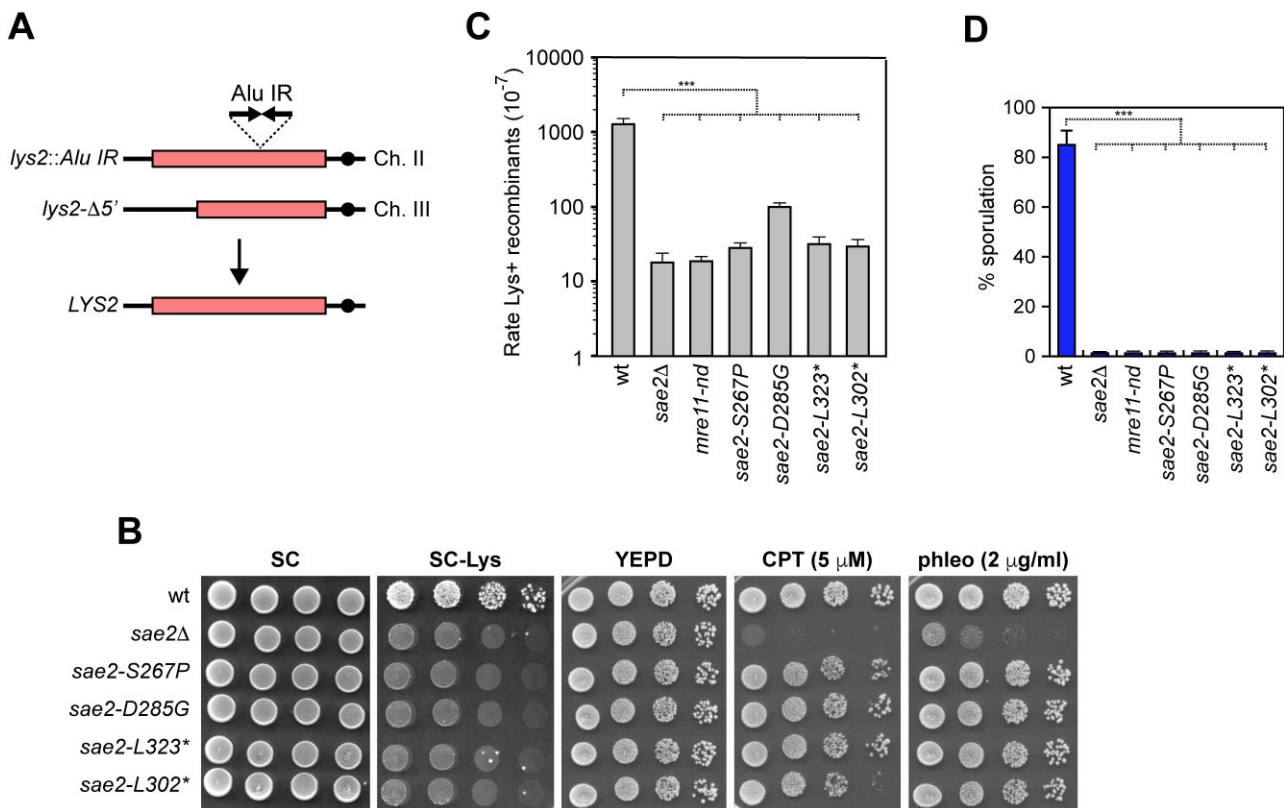
Figure 1. Search for *sae2* mutants defective in hairpin resolution. (**A**) Schematic representation of the *lys2::Alu IR* and *lys2-Δ5'* ectopic recombination system. (**B**) Exponentially growing cultures were serially diluted, and each dilution was spotted out on SC medium with or without lysine and on yeast extract, bactopeptone, and glucose (YEPD) plates with or without CPT or phleomycin. (**C**) Recombination frequency of strains with the *lys2::Alu IR* and *lys2-Δ5'* ectopic recombination system. The rate of Lys+ recombinants was derived from the median recombination frequency. The mean values of three independent experiments are represented with error bars denoting s.d. ***$P < 0.005$ (Student's *t*-test). (**D**) Percentage of sporulation. Diploid cells homozygous for the indicated mutations were induced to enter meiosis. The mean values of three independent experiments are represented with error bars denoting s.d. ***$P < 0.005$ (Student's *t*-test).

role of the C-terminal part of Sae2 in stimulation of MRX endonuclease activity. To further investigate the function of the Sae2 C-terminus, we focused on the *sae2-L323** allele (hereafter referred to as *sae2-ΔC23*), in which a stop codon replaces Leu323, thereby eliminating the last 23 amino acids of the protein. This truncation did not reduce the protein stability, as we detected comparable levels of Sae2 and Sae2^ΔC23 in protein extracts (Figure 2A). Furthermore, the Sae2^ΔC23 mutant variant maintained the ability to interact with the MRX complex. In fact, by expressing epitope-tagged versions of Rad50, Sae2, and Sae2^ΔC23 from their native genomic loci and immunoprecipitating Rad50-hemagglutinin (HA) fusion protein with an anti-HA antibody, we detected similar amounts of Sae2-Myc and Sae2^ΔC23-Myc in the HA-tagged Rad50 immunoprecipitates (Figure 2B).

While the Mre11 endonuclease activity is crucial for removing hairpin-capped DSBs or protein blocks (27,28), it becomes dispensable for resecting DSBs induced by endonucleases, where the DNA ends are readily accessible to Exo1 and Dna2 nucleases (29). Conversely, the absence of Sae2 impairs the resection of endonuclease-induced DSBs by increasing Rad9 binding at DSB sites, which subsequently inhibits the resection activities of Dna2 and Exo1 (48–51). If the primary function of the Sae2 C-terminus is to stimulate Mre11 endonuclease activity, then the *sae2-ΔC23* mutant would be expected to support resection of an endonuclease-induced DSB effectively. To assess the resection capability of *sae2-*

ΔC23 cells, we monitored the formation of ssDNA at an HO-induced DSB in JKM139 derivative strains, which express the HO endonuclease gene under a galactose-inducible promoter (60). Induction of HO by galactose addition results in the generation of a single DSB at the *MAT* locus, a break that cannot be repaired by HR due to the deletion of the homologous donor loci *HML* and *HMR*. Resection of this HO-induced DSB makes the DNA sequences flanking the break resistant to cleavage by restriction enzymes, allowing the detection of resection intermediates by Southern blot using a probe that anneals to the 3' end on one side of the break. As expected, *sae2Δ* cells showed a resection defect compared to wild-type cells, whereas wild-type and *sae2-ΔC23* cells accumulated resection products with similar kinetics (Figure 2C and D).

The DSB resection defect observed in *sae2Δ* cells partially explains their decreased resistance to CPT compared to *mre11-nd* cells, which are sensitive only to higher CPT doses. Consequently, if the absence of the Sae2 C-terminus impacts Mre11 nuclease activity, then the *sae2-ΔC23* mutant would be expected to exhibit DNA damage sensitivity similar to that of *mre11-nd*. Our results confirmed this hypothesis, as both *sae2-ΔC23* and *mre11-nd* cells displayed comparable sensitivity to CPT (Figure 2E). Furthermore, the *sae2-ΔC23* allele did not exacerbate the DNA damage sensitivity observed in *mre11-nd* cells (Figure 2E).

Previous studies have shown that the *sae2Δ* mutation results in lethality when combined with the *SGS1* deletion, while
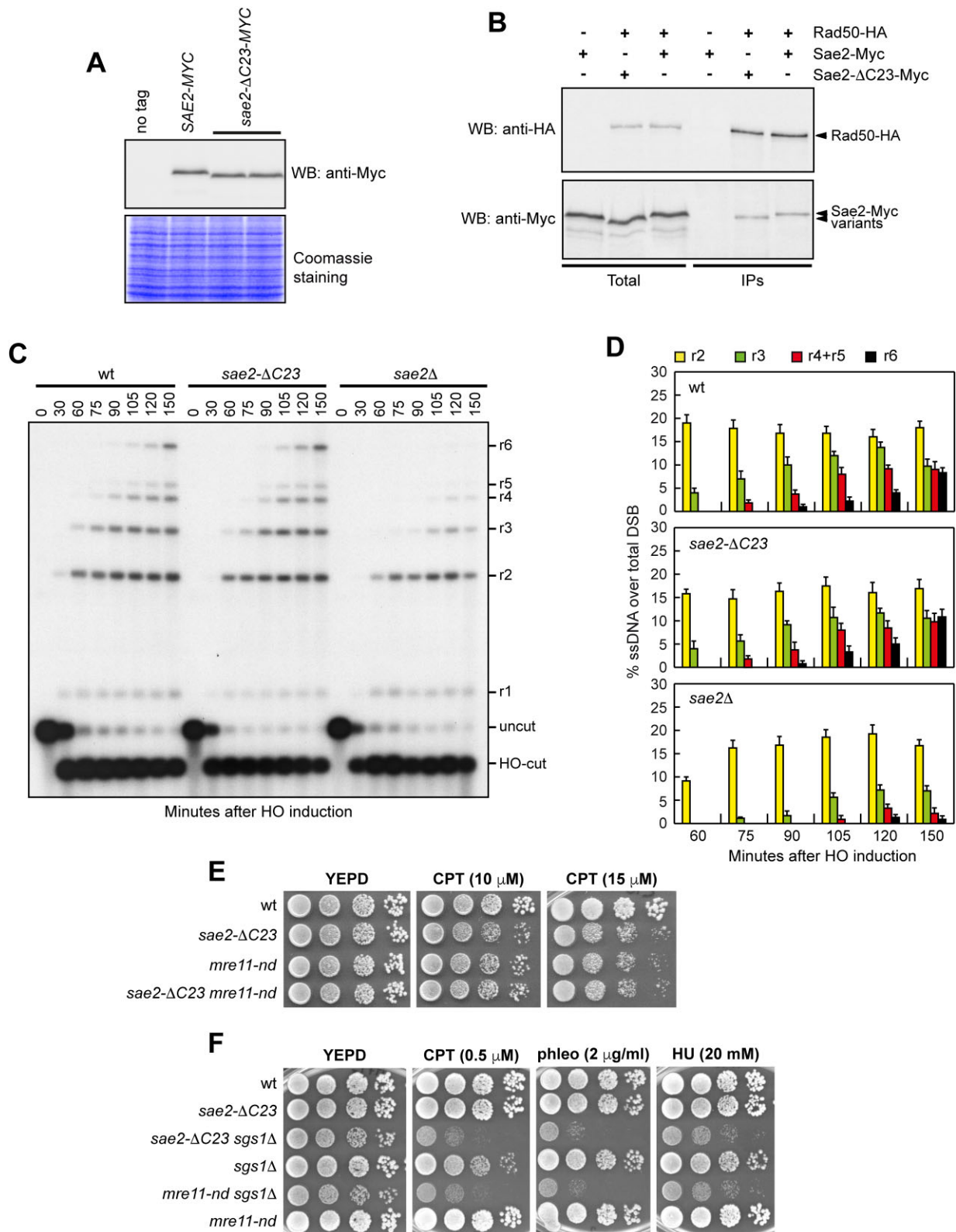
Figure 2. The *sae2-ΔC23* mutation does not impair resection of an endonuclease-induced DSB. (**A**) Western blot analysis with an anti-Myc antibody of protein extracts prepared from exponentially growing cells. The same amount of extracts was stained with Coomassie Blue as loading control. (**B**) Co-IP. Protein extracts from exponentially growing cells were analyzed by western blotting with anti-HA and anti-Myc antibodies either directly (Total) or after IPs of Rad50-HA with an anti-HA antibody. (**C**) DSB resection. JKM139 derivative strains were transferred from YEPR to YEPRG at time zero. *Ssp*I-digested genomic DNA was hybridized with a single-stranded *MAT* probe that anneals with the unresected strand. 5′-3′ resection produces *Ssp*I fragments (r1 to r6) detected by the probe. (**D**) Densitometric analysis of the resection products. The mean values of three independent experiments as in (**C**) are represented with error bars denoting s.d. (**E, F**) Exponentially growing cells were serially diluted and each dilution was spotted out onto YEPD plates with or without CPT, phleomycin or HU at the indicated concentrations.

the *mre11-nd sgs1Δ* double mutant is viable, although with a slight growth defect and increased DNA damage sensitivity compared to each single mutant (51). We found that the *sae2-ΔC23* allele, similarly to *mre11-nd*, was viable in combination with *sgs1Δ* and exacerbated its DNA damage sensitivity, consistent with a defect in the activation of Mre11 endonuclease (Figure 2F).

The lack of the Sae2 C-terminus maintains Sae2 function in inhibiting Rad53 activation

Both *sae2Δ* and *mre11-nd* cells exhibit elevated levels of Mre11 and Tel1 at the DSBs (50,51). However, unlike *mre11-nd* cells, *sae2Δ* cells also show excessive accumulation of Rad9 near the DSB, leading to Rad53 hyperactivation (47–51), indicating that Sae2 inhibits Rad53 activation independently of its role in stimulating MRX nuclease activity. Thus, we used ChIP and quantitative PCR (qPCR) to analyze the association of Mre11, Tel1 and Rad9 with the HO-induced DSB in *sae2-ΔC23* cells. Although similar amounts of Mre11 (Figure 3A), Tel1 (Figure 3B) and Rad9 (Figure 3C) were detected in all protein extracts, *sae2Δ*, *mre11-nd* and *sae2-ΔC23* cells showed increased enrichment of both Mre11 and Tel1 near the HO-induced DSB (Figure 3D and E). By contrast, an increased accumulation of Rad9 was observed only in *sae2Δ* cells, while the levels of Rad9 bound at the HO-induced DSB in both *mre11-nd* and *sae2-ΔC23* were similar to those in wild-type cells (Figure 3F).

Since the increased Rad9 association with DSBs in *sae2Δ* cells leads to Rad53 hyperactivation, we expected similar levels of Rad53 activation in both wild-type and *sae2-ΔC23* cells. It is known that cells harboring a single irreparable DSB undergo checkpoint-mediated cell-cycle arrest, but subsequently decrease Rad53 activation and re-enter the cell cycle (61,62). The inability of *sae2Δ* cells to deactivate the checkpoint triggered by a single irreparable DSB (47) prompted us to analyze the adaptation response of *sae2-ΔC23* cells to such a DSB. When G1-arrested cell cultures of JKM139 derivative strains were spotted on galactose-containing plates to induce HO, most *sae2Δ* cells remained arrested at the two-cell dumbbell stage after 20 hours (Figure 3G). By contrast, both wild-type and *sae2-ΔC23* cells overcame the checkpoint-mediated cell-cycle arrest within 16 hours and formed microcolonies with more than two cells (Figure 3G). Furthermore, when galactose was added to exponentially growing cell cultures of these strains, Rad53 phosphorylation decreased in both wild-type and *sae2-ΔC23* cells 12–14 h after galactose addition, whereas it persisted in *sae2Δ* cells (Figure 3H). These findings indicate that *sae2-ΔC23* cells are capable of downregulating Rad53 activation.

As Sae2 has been shown to inhibit Rad53 activation by limiting the interaction between Rad53 and Rad9 (51,63), we immunoprecipitated HA-tagged Rad9 from cell extracts prepared from undamaged, exponentially growing cells. In wild-type cells, a very low basal level of Rad53 binding to Rad9 was detectable even in the absence of DNA damage (Figure 3I). This interaction increased when Rad9 was immunoprecipitated from *sae2Δ* cells, which also exhibited phosphorylated Rad53, indicating that Rad53 is hyperactivated in these cells (Figure 3I). In contrast, both *mre11-nd* and *sae2-ΔC23* cells showed Rad53 binding to Rad9 at levels similar to those observed in wild-type cells (Figure 3I). These findings indicate that the absence of the Sae2 C-terminus

does not impair Sae2 ability to inhibit the Rad53–Rad9 interaction.

AlphaFold3-based modeling of the Sae2 C-terminus bound to Rad50

To gain structural insights into the role of the C-terminus of Sae2 within the Mre11-Rad50 complex, we first employed AlphaFold2 Multimer 2.0, previously used to predict the structure of the Mre11–Rad50–Sae2 complex (64,65). We modeled the C-terminal region of Sae2 (amino acids 181–345) alongside Rad50, omitting the 214–1107 amino acid region of the Rad50 coiled-coil for computational efficiency. The phosphorylation of Sae2 at Ser267 is crucial for its interaction with Rad50 and for stimulating Mre11 endonuclease activity (40,42). However, because AlphaFold2 does not accommodate post-translational modifications, we substituted Ser267 with glutamic acid (S267E) to mimic constitutive phosphorylation, enabling a more stable interaction with the Rad50 interface. Our attempts to model the Mre11 endonuclease and capping domain (amino acids 1–416) consistently positioned the Mre11 subunit in a configuration resembling its resting state within the Mre11–Rad50–Sae2 complex. As a result, this configuration was not further pursued in our analysis. The AlphaFold2 model provided high-confidence predictions for the amino acid regions 202–216 and 264–345 of Sae2, with a segment of lower confidence between these regions (Supplementary Figure S1A and B). The model obtained is very similar to the one recently described (65), with an RMSD of 0.463 along the Sae2 portion.

Due to the limitations of AlphaFold2 in considering phosphorylation at S267 and its tendency to model the Mre11 subunit in a position similar to the resting state observed in the *E. coli* homolog complex (36,37), we utilized the updated version of this predictor, AlphaFold3, to model the 181–345 amino acid region of Sae2, phosphorylated at S267, along with Rad50 (again excluding the amino acid 214–1107 extension of the coiled-coil region) and Mre11 (amino acids 1–416). However, although the phosphomimetic glutamic acid substitution mutant (Sae2-S267E) supported MRX-dependent DNA cleavage, its activity has been shown to decrease after treatment with λ phosphatase (66). This finding suggests that additional phosphorylation sites on Sae2 are necessary for optimal MRX endonuclease activity. Sae2 is phosphorylated not only by CDKs but also by the checkpoint kinases Mec1 and Tel1 (38,39,43), whose ATR and ATM orthologs phosphorylate the conserved T818 residue of *Xenopus laevis* CtIP (equivalent to T279 of Sae2 and T859 of human CtIP) (67,68). Interestingly, the non-phosphorylatable substitution of Sae2 T279A significantly reduced Spo11 release more severely than the corresponding phosphomimetic T279E mutation (66). This finding prompted us to predict the structure of the Rad50-Mre11-Sae2 assembly with Sae2 phosphorylated at both S267 and T279.

AlphaFold3 successfully prioritized the positioning of the Mre11 subunit in a configuration resembling the active cutting state (Figure 4A and B), particularly when the Sae2 chain was phosphorylated on both S267 and T279 residues. This likely resulted in a higher score due to additional stabilization from salt bridge interactions involving phosphorylated S267 with Mre11, which reduced free energy. Phosphorylation on residue T279 was also mandatory for Alphafold3 to construct the model in cutting state.
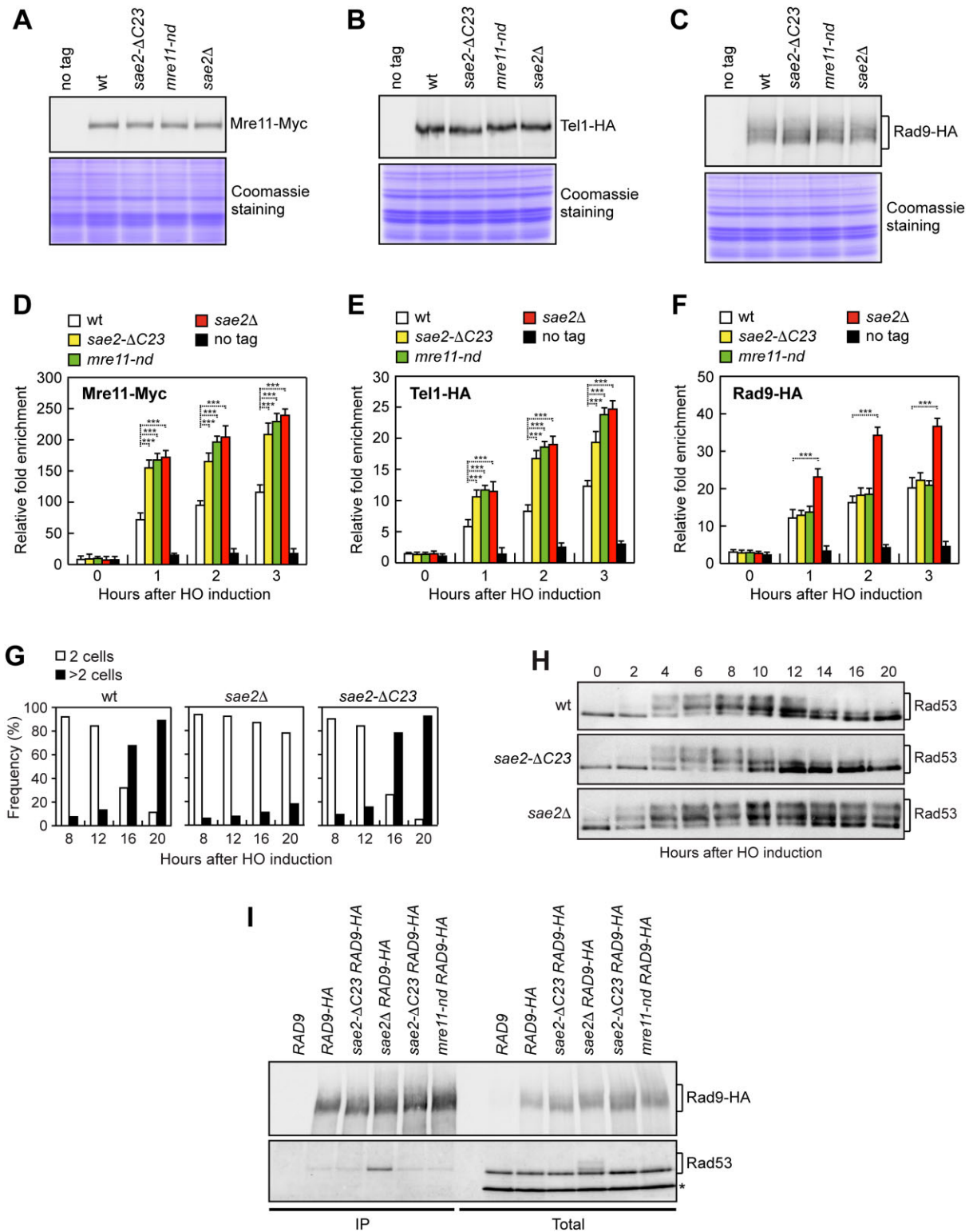
Figure 3. The *sae2-ΔC23* mutation enhances Mre11 and Tel1, but not Rad9 association with DSBs. (**A–C**) Western blot analysis with anti-Myc or anti-HA antibodies of protein extracts prepared from exponentially growing cells. The same amount of extracts was stained with Coomassie Blue as loading control. (**D–F**) ChIP and qPCR. Exponentially growing YEPR cell cultures were transferred to YEPRG to induce HO expression, followed by ChIP analysis of the recruitment of the indicated proteins at 600 bp from the HO-cut site. In all diagrams, ChIP signals were normalized to the corresponding input signal for each time point. The mean values of three independent experiments are represented with error bars denoting s.d. ***$P < 0.005$ (Student's *t*-test). (**G**) Adaptation assay. YEPR G1-arrested cell cultures were plated on galactose-containing plates (time zero). At the indicated time points, 200 cells for each strain were analyzed to determine the frequency of large, budded cells (two cells) and cells forming microcolonies of more than two cells (>2 cells). (**H**) Exponentially growing YEPR cell cultures were transferred to YEPRG at time zero to induce HO. Western blot analysis of protein extracts was performed with anti-Rad53 antibodies. (**I**) Co-IP. Protein extracts prepared from exponentially growing cells were analyzed by western blotting with anti-HA (Rad9) and anti-Rad53 antibodies either directly (Total) or after IP of Rad9-HA with an anti-HA antibody. *indicates a cross-hybridization signal.
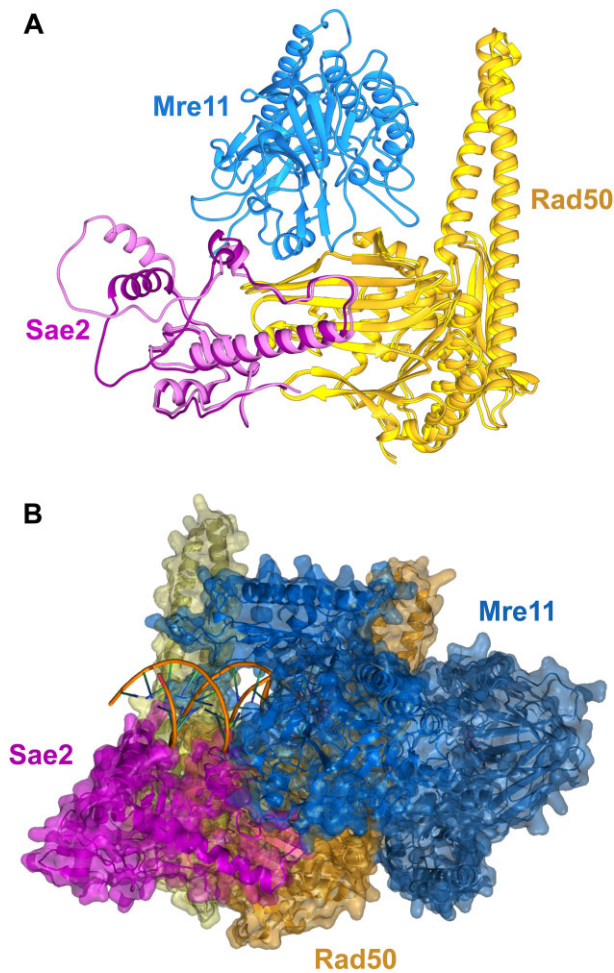
Figure 4. AlphaFold-based models for Sae2 C-terminal region binding to Rad50 and Mre11. (**A**) Cartoon representation of the 202–345 amino acid region of Sae2 (in magenta) phosphorylated at S267 and T279 residues, as modeled by AlphaFold3 server, together with Rad50 (in gold and with the aa 214–1107 coiled-coil region deleted), and Mre11 (aa 1–416, in blue) was superimposed on the AlphaFold2 model of Sae2 S267E (in pink) and Rad50 (in light yellow) for comparative analysis. (**B**) Model of the cutting state for Mre11–Rad50–Sae2 complex bound to DNA. The proteins are represented as cartoons with transparent surfaces, while the DNA molecule is depicted as a cartoon. Mre11 subunits are displayed in different shades of blue, Rad50 in yellow and light orange, and Sae2 in magenta.

The RMSD between the Sae2 portions of the Alphafold2 and Alphafold3 models is very low, at 0.510, indicating that both predictors constructed a highly similar structure for Sae2 (Figure 4A). A comparison of the Sae2 C-terminal conformation between the updated AlphaFold3 model and previous AlphaFold2 predictions (Figure 4A) shows that the amino acid region 264–345 is similarly predicted and maintains a high-confidence pLDDT score. In contrast, the region preceding amino acid 264 exhibits a lower confidence score (Supplementary Figure S1C and D) and diverges from the AlphaFold2 prediction, suggesting greater flexibility in this part of Sae2 (Figure 4A). The positioning of Mre11 relative to Rad50 remains consistent with the active cutting state of the Mre11–Rad50 complex, closely matching the resolved structure of the *E. coli* homologous complex (PDB ID: 7Z03) (Figure 4B).

Similarly to the AlphaFold2 prediction, the region from amino acid 264 to the C-terminus of Sae2 orients toward the ATPase domain β-sheet of Rad50 (Figure 5A). The phosphorylated S267 (pS267) residue allows the formation of a salt bridge with R77 in Rad50 and R187 in Mre11 (Figure 5B), confirming the structural basis for the previously described regulatory impact of CDK-dependent phosphorylation at S267 (40,42,65). Interactions are also predicted between Sae2 residue K296 and Rad50 N18 (Figure 5B), a residue previously identified as playing a key role in regulating Rif2 versus Sae2 binding to the overlapping interface in Rad50 protein (45).

Interestingly, the ATPase domain β-sheet of Rad50 is known to be altered by the *rad50-s* mutations (Figure 5B and C) (44), potentially explaining the phenotypes of the *rad50-s* mutants. Specifically, the D285 residue in Sae2, identified in this study, forms a salt bridge with the R20 residue in Rad50, which is also mutated in the *rad50-s* alleles (Figure 5B). Additionally, phosphorylated T279 in Sae2 was predicted to interact with K6, a residue affected by a *rad50-s* mutation (Figure 5B). When we substituted the T279 residue with a non-phosphorylatable alanine residue, *sae2-T279A* cells resulted in a decreased rate of Lys+ recombinants compared to wild-type cells (Figure 6A), whereas the phosphomimetic glutamic acid substitution, *sae2-T279E*, did not show this defect but rather increased the recombination rate compared to wild-type cells (Figure 6A), suggesting that this variant might be even more active than the wild-type counterpart. Similar to *sae2-S267A* cells, both *sae2-T279A* and *sae2-T279E* cells did not show an increased CPT sensitivity compared to wild-type cells (Figure 6B).

Another site affected by *rad50-s* mutations, E21, together with D19, was predicted to directly interact with the R344 residue in the Sae2 C-terminus (Figure 6C). When we substituted the R344 residue in Sae2 or its Rad50 binding partners, D19 and E21, with alanine, the *sae2-R344A* and *rad50-D19A, E21A* mutations led to decreased rates of Lys+ recombinants compared to wild-type cells, with *rad50-D19A, E21A* showing a reduction similar to that observed in *mre11-nd* cells (Figure 6D). Consistent with a more severe endonucleolytic defect, cells harboring the *rad50-D19A, E21A* allele were as sensitive to CPT and phleomycin as *mre11-nd* cells, whereas the DNA damage sensitivity of *sae2-R344A* cells remained comparable to wild-type cells (Figure 6E). This relatively milder phenotype of *sae2-R344A* cells might be explained by the presence of another positively charged residue, K286 in Sae2, located near Rad50 D19 and E21 and interacting with E21, which could potentially compensate for the absence of R344 (Figure 6C). Supporting this hypothesis, cells containing both K286A and R344A mutations exhibited decreased rates of Lys+ recombinants compared to wild-type cells, with a reduction similar to that observed in *rad50-D19A, E21A* cells (Figure 6D). Furthermore, the presence of the K286A mutation increased the CPT sensitivity of *sae2-R344A* cells to a level similar to *rad50-D19A, E21A* cells (Figure 6E).

Evaluation of the Sae2 and Rad50 interface by targeted mutagenesis

AlphaFold3 modeling suggests that the C-terminus of Sae2 is directly involved in multiple interactions with the Rad50 interface. These contacts are crucial for maintaining the stable binding necessary for a functional cutting-state configuration,
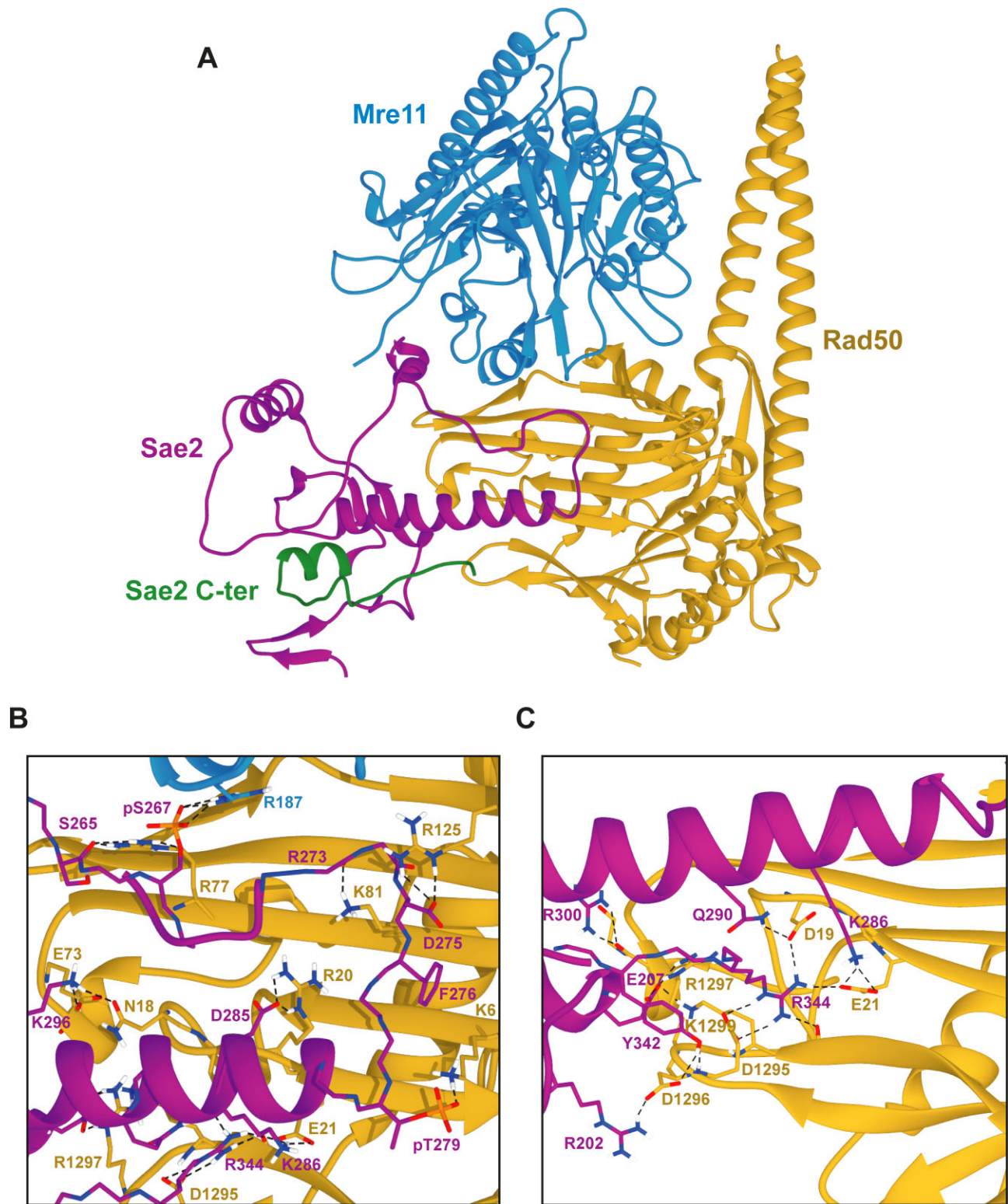
Figure 5. AlphaFold3-based model for Sae2 C-terminal region binding to Rad50. (**A**) Cartoon representation of the Sae2 202–345 amino acid region containing the phosphorylated Sae2 S267 and T279 residues, as modeled by the AlphaFold3 algorithm, together with Rad50, from which the amino acid 214–1107 coiled-coil region has been omitted, and Mre11 (aa 1–416). (**B,C**) The polar interactions between the Sae2 chain and the Rad50 chain are represented as a cartoon. Residues involved in contacts are represented as sticks and H-bonds are represented as dashed black lines. Nitrogen atoms are colored in blue, oxygen in red, and hydrogen in white. The view is rotated by 90° on the *Y*-axis from panel **B** to panel **C**.
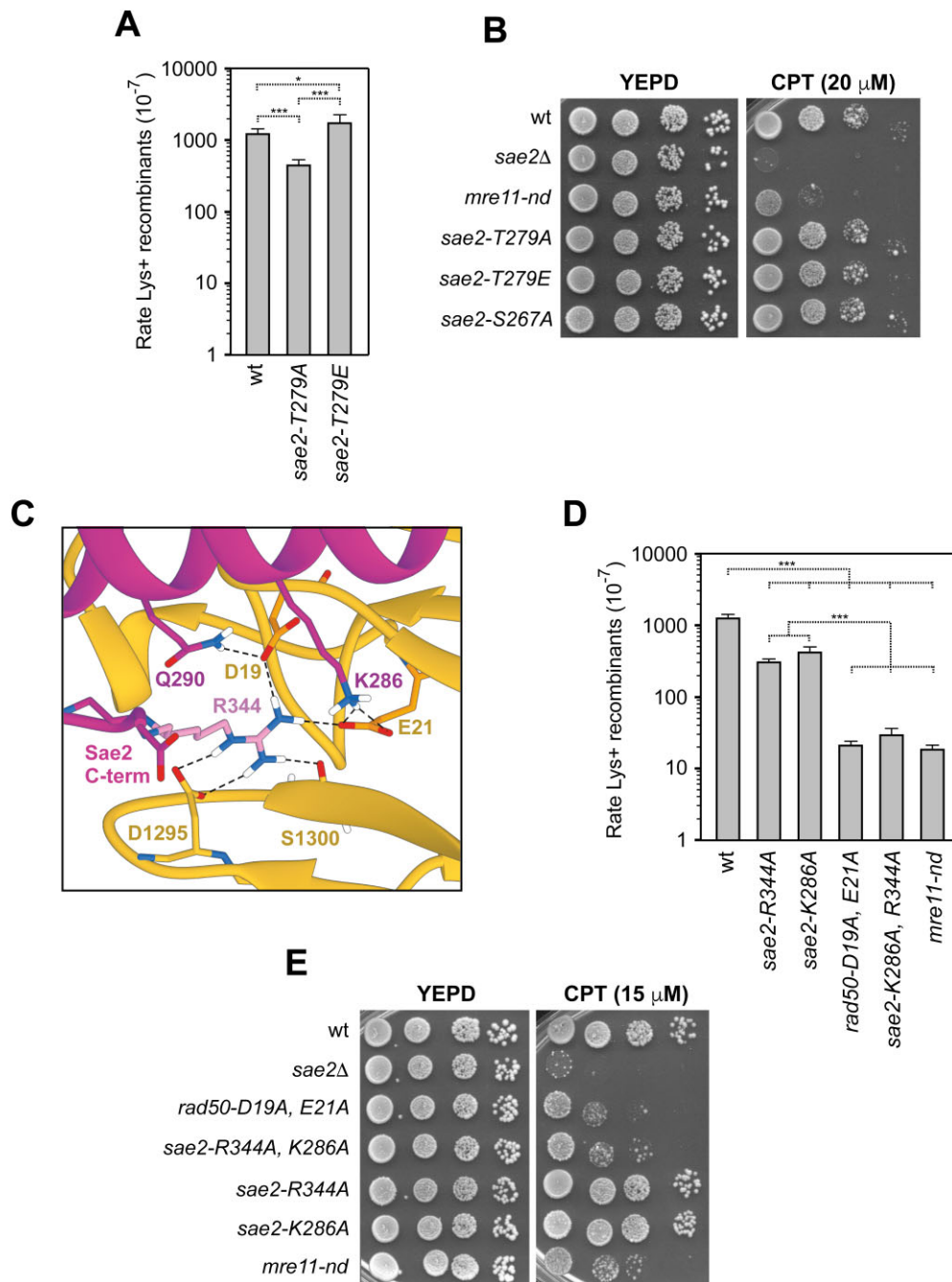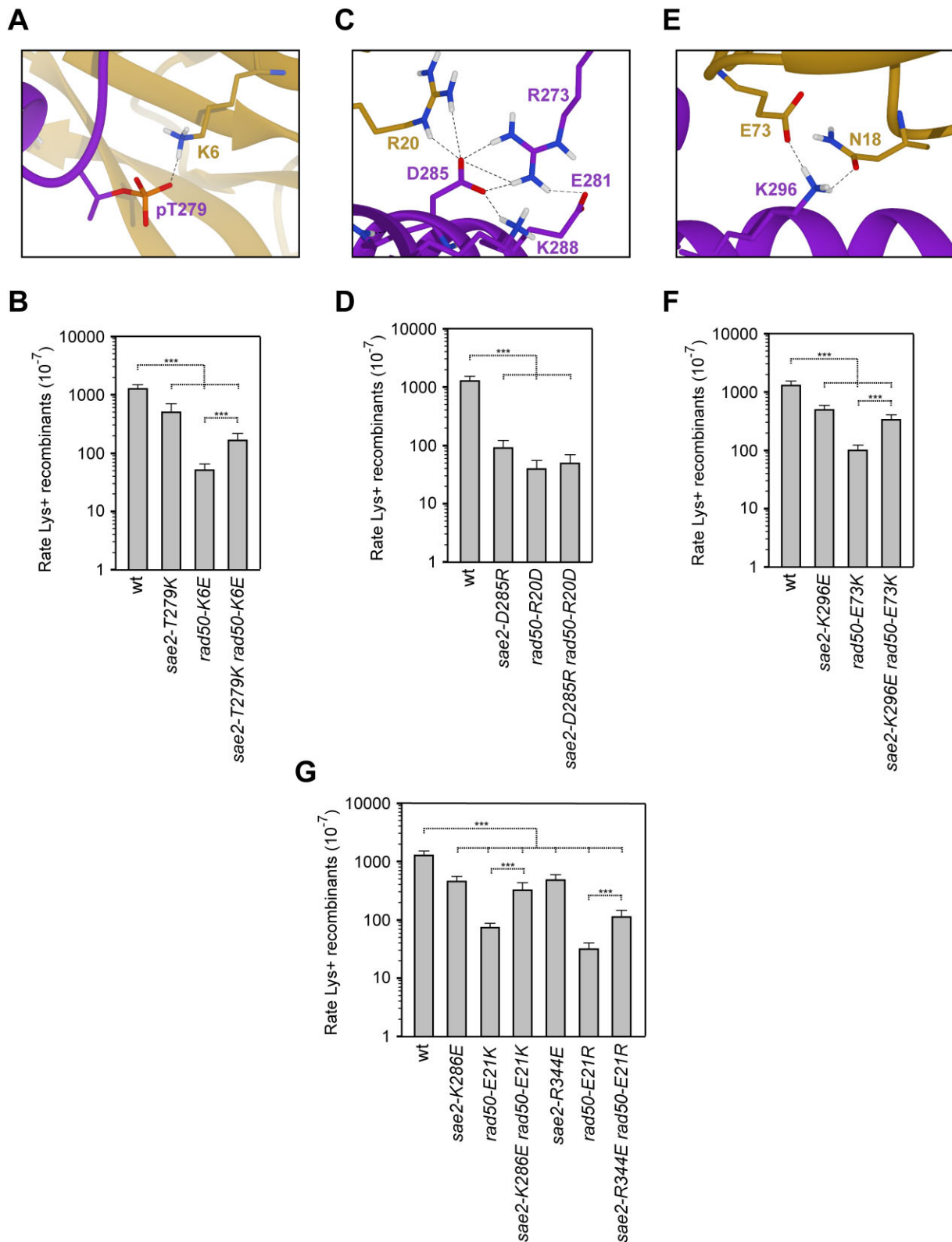
Figure 6. The binding site of the Sae2 C-terminus and relative mutations. (**A**) Recombination frequency of strains with the *lys2::Alu IR* and *lys2-Δ5'* ectopic recombination system. The rate of Lys+ recombinants was derived from the median recombination frequency. The mean values of three independent experiments are represented with error bars denoting s.d. *$P < 0.05$, ***$P < 0.005$ (Student's *t*-test). (**B**) Exponentially growing cultures were serially diluted, and each dilution was spotted out on YEPD plates with or without CPT. (**C**) Details of the binding site of the C-terminus of Sae2 with Rad50. The polar contacts of R286 and R344 of Sae2 and D19 and E21 of Rad50, targeted for mutation and highlighted in pink (Sae2) and orange (Rad50), are shown as black dashed lines. (**D**) As in A. (**E**) Exponentially growing cultures were serially diluted, and each dilution was spotted out on YEPD plates with or without CPT.

which may explain the phenotypes observed in *sae2* mutants lacking the C-terminus. To test these predictions, we introduced specific mutations and assessed their potential compensatory effects by comparing the rate of Lys+ recombinants of the double mutant with that of the single mutation showing the greatest reduction in recombination (65).

We first evaluated the predicted interaction between phosphorylated T279 in Sae2 and the K6 residue in Rad50 (Figure 7A) by substituting the negatively charged Sae2 T279 (in its phosphorylated form) with K (T279K) and analyzing the resulting phenotypes both individually and in combination with the charge-reversal variant K6E in Rad50. The single mutants *sae2-T279K* and *rad50-K6E* reduced the recombination rates compared to the wild type (Figure 7B), whereas the double mutant exhibited a recombination rate higher than that of the more severe *rad50-K6E* single mutant

Figure 7. Targeted mutagenesis and compensatory effects. (**A**) Details of the salt bridge between Sae2 phosphorylated residue T279 and Rad50 K6. (**B**) Recombination frequency of strains with the *lys2::Alu IR* and *lys2-Δ5'* ectopic recombination system. The rate of Lys⁺ recombinants was derived from the median recombination frequency. The mean values of three independent experiments are represented with error bars denoting s.d. ***$P < 0.005$ (Student's *t*-test). (**C**) Details of the complex network of polar interactions involving Sae2 D285, R273, K288 and E281, and Rad50 R20. (**D**) As in B. (**E**) Details of the polar interactions between the Sae2 K296 residue and Rad50 N18 and E73. (F,G) As in B. Residues involved in contacts are represented as sticks and polar interactions are represented as dashed black lines. Nitrogen atoms are colored in blue, oxygen in red, and hydrogen in white.

(Figure 7B), supporting the predicted interaction between T279 and K6.

Next, we investigated the potential salt bridge between the negatively charged D285 in Sae2 and the positively charged R20 in Rad50 (Figure 7C), by substituting D285 with R and introducing the corresponding charge-reversal R20D mutation in Rad50. The double mutant, however, exhibited a recombination rate similar to that of the equally deleterious *rad50-R20D* single mutant (Figure 7D), indicating no compensatory effect. This finding suggests that either the two residues do not interact in a manner that can be rescued by simple charge reversal, or that additional structural constraints prevent the formation of a compensatory interaction. Supporting this latter hypothesis, the analysis of the intramolecular interactions involving D285 residue reveals a complex network of H-bonds and salt bridges with Sae2 R273, E281 and K288 residues, likely involved in the proper folding of Sae2 and seriously affected by *sae2-D285R* mutation leading to the severe defect of the mutant (Figure 7C) (65).

Additionally, we explored the interaction between K296 in Sae2 and E73 in Rad50 (Figure 7E). Substituting the positively charged K296 with a negatively charged glutamic acid, along with the charge-reversal mutation *rad50-E73K*, resulted in a double mutant with a recombination rate higher than that of the more severe *rad50-E73K* single mutant (Figure 7F), indicating a compensatory effect that supports the predicted interaction between K296 and E73.

A similar effect was observed between the negatively charged E21 residue in Rad50 and the positively charged K286 and R344 residues in Sae2 (Figure 6C). In fact, when E21 in Rad50 was replaced by K, along with the charge-reversal mutation K286E in Sae2, the double mutant showed higher recombination rates compared to the *rad50-E21K* single mutant (Figure 7G). Likewise, substituting E21 in Rad50 with R, in combination with the charge-reversal mutation R344E in Sae2, resulted in improved recombination compared to the single *rad50-E21R* mutant (Figure 7G), thus supporting the predicted interactions.

Discussion

In both yeast and mammals, Sae2/CtIP stimulates Mre11 activity within the MRX complex, enabling endonucleolytic cleavage of secondary DNA structures and the 5′-terminated strands at DSBs, beyond various covalently or non-covalently bound proteins. This regulatory function is mediated by the direct physical interaction between Sae2 and Rad50, which depends on the phosphorylation of the Sae2 S267 residue (40,42,65). Recently, this Sae2 phosphorylated site was shown to make direct contact also to R187 of Mre11 in the endonuclease-competent cutting state of the Mre11–Rad50–Sae2 complex (65). Additionally, Sae2 negatively regulates checkpoint activation, independently of its role in stimulating MRX endonuclease activity, and this function helps to mitigate the inhibition of resection exerted by Rad9 and Rad53 on Exo1 and Dna2-Sgs1 activities (46–51).

By studying *sae2* mutants specifically impaired in processing hairpin-capped DNA ends, we identified mutations leading to deletions of portions of the Sae2 C-terminus. Focusing on the allele that causes the shorter deletion, we showed that the loss of the last 23 amino acids of Sae2 specifically impairs Sae2 ability to support MRX activity, while still allowing it to regulate checkpoint activation and to promote the resection activities of Exo1 and Dna2-Sgs1. This highlights the critical role of the C-terminal region of Sae2 in stimulating Mre11 activity, supported by previous findings showing that a Sae2 mutant lacking the last 95 amino acids fails to promote MRX endonuclease activity *in vitro* (66).

Using the AlphaFold3 predictor to model the Sae2 C-terminus bound to Rad50, we discovered that the region spanning amino acids 264 to the C-terminus of Sae2 is predicted to interact with the β-sheet of Rad50 ATPase domain. Notably, this Rad50 region harbors the *rad50-s* mutations, with the prototypical *rad50-K81I* mutant failing to interact with phosphorylated Sae2 and to stimulate Mre11-Rad50 endonuclease activity (42). Our model reveals that many of the interactions between Sae2 and Rad50 occur far downstream of the S267 phosphorylation site. This network of interactions is crucial for stabilizing the association between Sae2 and Rad50, thereby allowing the correct positioning of Mre11 in its active, cutting state.

According to AlphaFold3 predictions, the phosphorylated S267 residue of Sae2 directly faces the 182–190 amino acid helix of Mre11, suggesting that phosphorylated S267 serves as a critical bridge between Rad50 and Mre11, enabling the proper conformation for endonucleolytic activity, as previously suggested (65). Interestingly, the Mre11 182–190 amino acid helix contains the T188 residue, which is altered by the *mre11-s* mutation. This mutation mimics the phenotype of *rad50-s* mutants, further underscoring the interconnected nature of these molecular interactions (69,70). Other Sae2 residues near phosphorylated S267, such as R264, which is a pivotal Mre11 bridging site, and D275, which anchors Sae2 to Rad50 R125 (65), were recently identified as necessary for Mre11 endonucleolytic activity (65).

Notably, our model predicts that, along with S267, the phosphorylation of T279 is also crucial for the Sae2–Rad50 interaction and Mre11 nuclease activity. Consistent with this prediction, a *sae2* mutant with a non-phosphorylatable T279 exhibited a reduced recombination rate, whereas recombination was restored in the corresponding phospho-mimetic *sae2* mutant. Similar results have been observed in meiosis, where *sae2-T279A* cells impaired Spo11 release more severely than cells carrying the phospho-mimetic mutation (66). While S267 is a known CDK target, T279 has been shown to be phosphorylated by Mec1 and Tel1, suggesting that Mre11 activity can also be modulated by the checkpoint pathway. Consistent with this hypothesis, the absence of both Mec1 and Tel1 leads to the accumulation of unprocessed DSBs in meiosis (39).

Given the critical role of multiple interactions involving Rad50 and the C-terminus of Sae2 in ensuring MRX endonuclease functionality, we sought to determine if the role of the Sae2 C-terminus is conserved across the diverse group of Sae2 orthologs. To this end, we used the AlphaFold3 predictor to model the human Mre11–Rad50 complex in its cutting state (Supplementary Figure S3A and B). Although mammalian CtIP lacks sequence conservation with yeast Sae2 (Supplementary Figure S3C), the model suggests a similar function for the phosphorylated T847 and T859 residues in CtIP, as for the phosphorylated S267 and T279 in yeast Sae2 (Supplementary Figure S3A). In this model, CtIP acts as a bridge between Rad50 and Mre11, stabilizing Mre11 position where its catalytic site is correctly aligned with the DNA (Supplementary Figure S3B). However, the folding of the more terminal portion of CtIP markedly differs from that of Sae2, as

expected from the sequence divergence in this region among orthologous proteins (Supplementary Figure S3C). Interestingly, the model predicts that the C-terminus of CtIP rests against the C-terminal region of Rad50, suggesting multiple interactions between this part of CtIP and human Rad50 as well. Thus, although Sae2 and CtIP may have undergone structural reorganization during evolution, their ability to stabilize the active conformation of MRX could be conserved. Consequently, the analysis reported here will be important for understanding the interplay between MRN and CtIP, whose dysfunction is linked to various human pathologies.

Data availability

All relevant data are included in the manuscript and the Supplementary Data file. Any other data are available from the authors on request.

Supplementary data

Supplementary Data are available at NAR Online.

Acknowledgements

Funding

Conflict of interest statement

None declared.

References

1. Stinson,B.M. and Loparo,J.J. (2021) Repair of DNA double-strand breaks by the nonhomologous end joining pathway. *Annu. Rev. Biochem.*, **90**, 137–164.
2. Mehta,A. and Haber,J.E. (2014) Sources of DNA double-strand breaks and models of recombinational DNA repair. *Cold Spring Harb. Perspect. Biol.*, **6**, a016428.
3. Cejka,P. and Symington,L.S. (2021) DNA end resection: mechanism and control. *Annu. Rev. Genet.*, **55**, 285–307.
4. Pizzul,P., Casari,E., Gnugnoli,M., Rinaldi,C., Corallo,F. and Longhese,M.P. (2022) The DNA damage checkpoint:a tale from budding yeast. *Front. Genet.*, **13**, 995163.
5. Gilbert,C.S., Green,C.M. and Lowndes,N.F. (2001) Budding yeast Rad9 is an ATP-dependent Rad53 activating machine. *Mol. Cell*, **8**, 129–136.
6. Schwartz,M.F., Duong,J.K., Sun,Z., Morrow,J.S., Pradhan,D. and Stern,D.F. (2002) Rad9 phosphorylation sites couple Rad53 to the *Saccharomyces cerevisiae* DNA damage checkpoint. *Mol. Cell*, **9**, 1055–1065.
7. Sweeney,F.D., Yang,F., Chi,A., Shabanowitz,J., Hunt,D.F. and Durocher,D. (2005) *Saccharomyces cerevisiae* Rad9 acts as a Mec1 adaptor to allow Rad53 activation. *Curr. Biol*, **15**, 1364–1375.
8. Syed,A. and Tainer,J.A. (2018) The MRE11-RAD50-NBS1 complex conducts the orchestration of damage signaling and outcomes to stress in DNA replication and repair. *Annu. Rev. Biochem.*, **87**, 263–294.
9. Paull,T.T. and Gellert,M. (1998) The 3′ to 5′ exonuclease activity of Mre 11 facilitates repair of DNA double-strand breaks. *Mol. Cell*, **1**, 969–979.
10. Trujillo,K.M., Yuan,S.S., Lee,E.Y. and Sung,P. (1998) Nuclease activities in a complex of human recombination and DNA repair factors Rad50, Mre11, and p95. *J. Biol. Chem.*, **273**, 21447–21450.
11. Usui,T., Ohta,T., Oshiumi,H., Tomizawa,J., Ogawa,H. and Ogawa,T. (1998) Complex formation and functional versatility of Mre11 of budding yeast in recombination. *Cell*, **95**, 705–716.
12. Hopfner,K.P., Karcher,A., Craig,L., Woo,T.T., Carney,J.P. and Tainer,J.A. (2001) Structural biochemistry and interaction architecture of the DNA double-strand break repair Mre11 nuclease and Rad50-ATPase. *Cell*, **105**, 473–485.
13. Seifert,F.U., Lammens,K., Stoehr,G., Kessler,B. and Hopfner,K.P. (2016) Structural mechanism of ATP-dependent DNA binding and DNA end bridging by eukaryotic Rad50. *EMBO J.*, **35**, 759–772.
14. Rotheneder,M., Stakyte,K., van de Logt,E., Bartho,J.D., Lammens,K., Fan,Y., Alt,A., Kessler,B., Jung,C., Roos,W.P., *et al.* (2023) Cryo-EM structure of the Mre11-Rad50-Nbs1 complex reveals the molecular mechanism of scaffolding functions. *Mol. Cell*, **83**, 167–185.
15. Hopfner,K.P., Craig,L., Moncalian,G., Zinkel,R.A., Usui,T., Owen,B.A., Karcher,A., Henderson,B., Bodmer,J.L., McMurray,C.T., *et al.* (2002) The Rad50 zinc-hook is a structure joining Mre11 complexes in DNA recombination and repair. *Nature*, **418**, 562–566.
16. Park,Y.B., Hohl,M., Padjasek,M., Jeong,E., Jin,K.S., Krężel,A., Petrini,J.H.J. and Cho,Y. (2017) Eukaryotic Rad50 functions as a rod-shaped dimer. *Nat. Struct. Mol. Biol.*, **24**, 248–257.
17. Mimitou,E.P. and Symington,L.S. (2008) Sae2, Exo1 and Sgs1 collaborate in DNA double-strand break processing. *Nature*, **455**, 770–774.
18. Zhu,Z., Chung,W.H., Shim,E.Y., Lee,S.E. and Ira,G. (2008) Sgs1 helicase and two nucleases Dna2 and Exo1 resect DNA double-strand break ends. *Cell*, **134**, 981–994.
19. Cejka,P., Cannavo,E., Polaczek,P., Masuda-Sasa,T., Pokharel,S., Campbell,J.L. and Kowalczykowski,S.C. (2010) DNA end resection by Dna2-Sgs1-RPA and its stimulation by Top3-Rmi1 and Mre11-Rad50-Xrs2. *Nature*, **467**, 112–116.
20. Niu,H., Chung,W.H., Zhu,Z., Kwon,Y., Zhao,W., Chi,P., Prakash,R., Seong,C., Liu,D., Lu,L., *et al.* (2010) Mechanism of the ATP-dependent DNA end-resection machinery from *Saccharomyces cerevisiae*. *Nature*, **467**, 108–111.
21. Nimonkar,A.V., Genschel,J., Kinoshita,E., Polaczek,P., Campbell,J.L., Wyman,C., Modrich,P. and Kowalczykowski,S.C. (2011) BLM-DNA2-RPA-MRN and EXO1-BLM-RPA-MRN constitute two DNA end resection machineries for human DNA break repair. *Genes Dev.*, **25**, 350–362.
22. Garcia,V., Phelps,S.E., Gray,S. and Neale,M.J. (2011) Bidirectional resection of DNA double-strand breaks by Mre11 and Exo1. *Nature*, **479**, 241–244.
23. Shibata,A., Moiani,D., Arvai,A.S., Perry,J., Harding,S.M., Genois,M.M., Maity,R., van Rossum-Fikkert,S., Kertokalio,A., Romoli,F., *et al.* (2014) DNA double-strand break repair pathway choice is directed by distinct MRE11 nuclease activities. *Mol. Cell*, **53**, 7–18.
24. Reginato,G., Cannavo,E. and Cejka,P. (2017) Physiological protein blocks direct the Mre11-Rad50-Xrs2 and Sae2 nuclease complex to initiate DNA end resection. *Genes Dev.*, **31**, 2325–2330.
25. Wang,W., Daley,J.M., Kwon,Y., Krasner,D.S. and Sung,P. (2017) Plasticity of the Mre11–Rad50–Xrs2–Sae2 nuclease ensemble in the processing of DNA-bound obstacles. *Genes Dev.*, **31**, 2331–2336.
26. Keeney,S., Giroux,C.N. and Kleckner,N. (1997) Meiosis-specific DNA double-strand breaks are catalyzed by Spo11, a member of a widely conserved protein family. *Cell*, **88**, 375–384.

27. Lobachev,K.S., Gordenin,D.A. and Resnick,M.A. (2002) The Mre11 complex is required for repair of hairpin-capped double-strand breaks and prevention of chromosome rearrangements. *Cell*, **108**, 183–193.

28. Neale,M.J., Pan,J. and Keeney,S. (2005) Endonucleolytic processing of covalent protein-linked DNA double-strand breaks. *Nature*, **436**, 1053–1057.

29. Llorente,B. and Symington,L.S. (2004) The Mre11 nuclease is not required for 5′ to 3′ resection at multiple HO-induced double-strand breaks. *Mol. Cell. Biol.*, **24**, 9682–9694.

30. Williams,G.J., Williams,R.S., Williams,J.S., Moncalian,G., Arvai,A.S., Limbo,O., Guenther,G., SilDas,S., Hammel,M., Russell,P., *et al.* (2011) ABC ATPase signature helices in Rad50 link nucleotide state to Mre11 interface for DNA repair. *Nat. Struct. Mol. Biol.*, **18**, 423–431.

31. Lammens,K., Bemeleit,D.J., Möckel,C., Clausing,E., Schele,A., Hartung,S., Schiller,C.B., Lucas,M., Angermüller,C., Söding,J., *et al.* (2011) The Mre11 structure shows an ATP-dependent molecular clamp in DNA double-strand break repair. *Cell*, **145**, 54–66.

32. Lim,H.S., Kim,J.S., Park,Y.B., Gwon,G.H. and Cho,Y. (2011) Crystal structure of the Mre11–Rad50–ATPγS complex: understanding the interplay between Mre11 and Rad50. *Genes Dev.*, **25**, 1091–1104.

33. Möckel,C., Lammens,K., Schele,A. and Hopfner,K.-P. (2012) ATP driven structural changes of the bacterial Mre11 catalytic head complex. *Nucleic Acids Res.*, **40**, 914–927.

34. Deshpande,R.A., Williams,G.J., Limbo,O., Williams,R.S., Kuhnlein,J., Lee,J.H., Classen,S., Guenther,G., Russell,P., Tainer,J.A., *et al.* (2014) ATP-driven Rad50 conformations regulate DNA tethering, end resection, and ATM checkpoint signaling. *EMBO J.*, **33**, 482–500.

35. Liu,Y., Sung,S., Kim,Y., Li,F., Gwon,G., Jo,A., Kim,A.K., Kim,T., Song,O., Lee,S.E., *et al.* (2016) ATP-dependent DNA binding, unwinding, and resection by the Mre11/Rad50 complex. *EMBO J.*, **35**, 743–758.

36. Käshammer,L., Saathoff,J.H., Lammens,K., Gut,F., Bartho,J., Alt,A., Kessler,B. and Hopfner,K.P. (2019) Mechanism of DNA end sensing and processing by the Mre11-Rad50 complex. *Mol. Cell*, **76**, 382–394.

37. Gut,F., Käshammer,L., Lammens,K., Bartho,J.D., Boggusch,A.M., van de Logt,E., Kessler,B. and Hopfner,K.P. (2022) Structural mechanism of endonucleolytic processing of blocked DNA ends and hairpins by Mre11-Rad50. *Mol. Cell*, **82**, 3513–3522.

38. Baroni,E., Viscardi,V., Cartagena-Lirola,H., Lucchini,G. and Longhese,M.P. (2004) The functions of budding yeast Sae2 in the DNA damage response require Mec1- and Tel1-dependent phosphorylation. *Mol. Cell. Biol.*, **24**, 4151–4165.

39. Cartagena-Lirola,H., Guerini,I., Viscardi,V., Lucchini,G. and Longhese,M.P. (2006) Budding yeast Sae2 is an in vivo target of the Mec1 and Tel1 checkpoint kinases during meiosis. *Cell Cycle*, **5**, 1549–1559.

40. Huertas,P., Cortés-Ledesma,F., Sartori,A.A., Aguilera,A. and Jackson,S.P. (2008) CDK targets Sae2 to control DNA-end resection and homologous recombination. *Nature*, **455**, 689–692.

41. Huertas,P. and Jackson,S.P. (2009) Human CtIP mediates cell cycle control of DNA end resection and double strand break repair. *J. Biol. Chem.*, **284**, 9558–9565.

42. Cannavo,E. and Cejka,P. (2014) Sae2 promotes dsDNA endonuclease activity within Mre11-Rad50-Xrs2 to resect DNA breaks. *Nature*, **514**, 122–125.

43. Yu,T.Y., Garcia,V.E. and Symington,L.S. (2019) CDK and Mec1/Tel1-catalyzed phosphorylation of Sae2 regulate different responses to DNA damage. *Nucleic Acids Res.*, **47**, 11238–11249.

44. Alani,E., Padmore,R. and Kleckner,N. (1990) Analysis of wild-type and *rad50* mutants of yeast suggests an intimate relationship between meiotic chromosome synapsis and recombination. *Cell*, **61**, 419–436.

45. Marsella,A., Gobbini,E., Cassani,C., Tisi,R., Cannavo,E., Reginato,G., Cejka,P. and Longhese,M.P. (2021) Sae2 and Rif2 regulate MRX endonuclease activity at DNA double-strand breaks in opposite manners. *Cell Rep.*, **34**, 108906.

46. Usui,T., Ogawa,H. and Petrini,J.H. (2001) A DNA damage response pathway controlled by Tel1 and the Mre11 complex. *Mol. Cell*, **7**, 1255–1266.

47. Clerici,M., Mantiero,D., Lucchini,G. and Longhese,M.P. (2006) The *saccharomyces cerevisiae* Sae2 protein negatively regulates DNA damage checkpoint signalling. *EMBO Rep.*, **7**, 212–218.

48. Bonetti,D., Villa,M., Gobbini,E., Cassani,C., Tedeschi,G. and Longhese,M.P. (2015) Escape of Sgs1 from Rad9 inhibition reduces the requirement for Sae2 and functional MRX in DNA end resection. *EMBO Rep.*, **16**, 351–361.

49. Ferrari,M., Dibitetto,D., De Gregorio,G., Eapen,V.V., Rawal,C.C., Lazzaro,F., Tsabar,M., Marini,F., Haber,J.E. and Pellicioli,A. (2015) Functional interplay between the 53BP1-ortholog Rad9 and the Mre11 complex regulates resection, end-tethering and repair of a double-strand break. *PLoS Genet.*, **11**, e1004928.

50. Gobbini,E., Villa,M., Gnugnoli,M., Menin,L., Clerici,M. and Longhese,M.P. (2015) Sae2 function at DNA double-strand breaks is bypassed by dampening Tel1 or Rad53 activity. *PLoS Genet.*, **11**, e1005685.

51. Yu,T.Y., Kimble,M.T. and Symington,L.S. (2018) Sae2 antagonizes Rad9 accumulation at DNA double-strand breaks to attenuate checkpoint signaling and facilitate end resection. *Proc. Natl. Acad. Sci. USA*, **115**, E11961–E11969.

52. Gnugnoli,M., Casari,E. and Longhese,M.P. (2021) The chromatin remodeler Chd1 supports MRX and Exo1 functions in resection of DNA double-strand breaks. *PLoS Genet.*, **17**, e1009807.

53. Rinaldi,C., Pizzul,P., Casari,E., Mangiagalli,M., Tisi,R. and Longhese,M.P. (2023) The Ku complex promotes DNA end-bridging and this function is antagonized by Tel1/ATM kinase. *Nucleic Acids Res.*, **51**, 1783–1802.

54. Colombo,C.V., Menin,L. and Clerici,M. (2018) Alkaline denaturing southern blot analysis to monitor double-strand break processing. *Methods Mol. Biol.*, **1672**, 131–145.

55. Casari,E., Gobbini,E., Clerici,M. and Longhese,M.P. (2021) Resection of a DNA double-strand break by alkaline gel electrophoresis and southern blotting. *Methods Mol. Biol. Clifton NJ.*, **2153**, 33–45.

56. Mirdita,M., Schütze,K., Moriwaki,Y., Heo,L., Ovchinnikov,S. and Steinegger,M. (2022) ColabFold: making protein folding accessible to all. *Nat. Methods*, **19**, 679–682.

57. Weiner,S.J., Kollman,P.A., Nguyen,D.T. and Case,D.A. (1986) An all atom force field for simulations of proteins and nucleic acids. *J. Comput. Chem.*, **7**, 230–252.

58. Pettersen,E.F., Goddard,T.D., Huang,C.C., Couch,G.S., Greenblatt,D.M., Meng,E.C. and Ferrin,T.E. (2004) UCSF Chimera–a visualization system for exploratory research and analysis. *J. Comput. Chem.*, **25**, 1605–1612.

59. Trujillo,K.M. and Sung,P. (2001) DNA structure-specific nuclease activities in the *Saccharomyces cerevisiae* Rad50*Mre11 complex. *J. Biol. Chem.*, **276**, 35458–35464.

60. Lee,S.E., Moore,J.K., Holmes,A., Umezu,K., Kolodner,R.D. and Haber,J.E. (1998) *Saccharomyces* Ku70, Mre11/Rad50, and RPA proteins regulate adaptation to G2/M arrest after DNA damage. *Cell*, **94**, 399–409.

61. Toczyski,D.P., Galgoczy,D.J. and Hartwell,L.H. (1997) CDC5 and CKII control adaptation to the yeast DNA damage checkpoint. *Cell*, **90**, 1097–1106.

62. Pellicioli,A., Lee,S.E., Lucca,C., Foiani,M. and Haber,J.E. (2001) Regulation of saccharomyces Rad53 checkpoint kinase during adaptation from DNA damage-induced G2/M arrest. *Mol. Cell*, **7**, 293–300.

63. Colombo,C.V., Menin,L., Ranieri,R., Bonetti,D., Clerici,M. and Longhese,M.P. (2019) Uncoupling Sae2 functions in downregulation of Tel1 and Rad53 signaling activities. *Genetics*, **211**, 515–530.

64. Myler,L.R., Toia,B., Vaughan,C.K., Takai,K., Matei,A.M., Wu,P., Paull,T.T., de Lange,T. and Lottersberger,F. (2023) DNA-PK and the TRF2 iDDR inhibit MRN-initiated resection at leading-end telomeres. *Nat. Struct. Mol. Biol.*, **30**, 1346–1356.

65. Nicolas,Y., Bret,H., Cannavo,E., Acharya,A., Cejka,P., Borde,V. and Guerois,R. (2024) Molecular insights into the activation of Mre11-Rad50 endonuclease activity by Sae2/CtIP. *Mol. Cell*, **84**, 2223–2237.

66. Cannavo,E., Johnson,D., Andres,S.N., Kissling,V.M., Reinert,J.K., Garcia,V., Erie,D.A., Hess,D., Thomä,N.H., Enchev,R.I., *et al.* (2018) Regulatory control of DNA end resection by Sae2 phosphorylation. *Nat. Commun.*, **9**, 4016.

67. Peterson,S.E., Li,Y., Wu-Baer,F., Chait,B.T., Baer,R., Yan,H., Gottesman,M.E. and Gautier,J. (2013) Activation of DSB processing requires phosphorylation of CtIP by ATR. *Mol. Cell*, **49**, 657–667.

68. Wang,H., Shi,L.Z., Wong,C.C., Han,X., Hwang,P.Y., Truong,L.N., Zhu,Q., Shao,Z., Chen,D.J., Berns,M.W., *et al.* (2013) The interaction of CtIP and Nbs1 connects CDK and ATM to regulate HR-mediated double-strand break repair. *PLoS Genet.*, **9**, e1003277.

69. Nairz,K. and Klein,F. (1997) *mre11S*–a yeast mutation that blocks double-strand-break processing and permits non homologous synapsis in meiosis. *Genes Dev.*, **11**, 2272–2290.

70. Tisi,R., Vertemara,J., Zampella,G. and Longhese,M.P. (2020) Functional and structural insights into the MRX/MRN complex, a key player in recognition and repair of DNA double-strand breaks. *Comput. Struct. Biotechnol. J.*, **18**, 1137–1152.